Volume 10
Number 8
28 February 2022
Pages 3825–4458

Journal of Materials Chemistry A

Materials for energy and sustainability

rsc.li/materials-a

ISSN 2050-7488

ROYAL SOCIETY OF CHEMISTRY

PAPER

Johnny C. Ho *et al.*

Sequential self-reconstruction of localized Mo species in hierarchical carbon/Co–Mo oxide heterostructures for boosting alkaline hydrogen evolution kinetics and durability

Journal of Materials Chemistry A

ROYAL SOCIETY OF CHEMISTRY

PAPER

View Article Online
View Journal | View Issue

Check for updates

Cite this: J. Mater. Chem. A, 2022, 10, 3953

Sequential self-reconstruction of localized Mo species in hierarchical carbon/Co–Mo oxide heterostructures for boosting alkaline hydrogen evolution kinetics and durability†

Quan Quan,[a] Xiuming Bu,[a] Dong Chen,[a] Fei Wang,[a] Xiaolin Kang,[a] Wei Wang,[a] You Meng,[a] SenPo Yip,[b] Chuntai Liu[c] and Johnny C. Ho *[abd]

Surface self-reconstruction processes in alkaline hydrogen evolution reaction (HER), especially regarding the explicit structure–activity relationships, remain elusive. Here, we first design a hierarchical Co@NCNT/$CoMoO_x$ precatalyst constituted by defective $CoMoO_x$ nanosheets grafted with flexible Co@NCNT arrays, followed by a delicate anodic treatment for fast dissolution balance. Benefiting from the multi-level Co@NCNT arrays as a stable micro-environment, the resultant Co@NCNT/$CoMo_yO_x$ displays excellent electrocatalytic activity with a low overpotential of 195 mV at −100 mA cm^{-2} and stable 600 h operation for the HER in alkaline media, including natural seawater, which is better than most reported carbon/transition metal-based catalysts. *In situ* Raman analyses disclose a local high-resolution self-reconstruction evolution of localized Mo species at controllable negative potentials. Density functional theory calculations further demonstrate that the ultimate Mo–Mo surface state accelerates reaction kinetics to promote H_2 generation in alkaline media. Our findings provide a unique insight into the mechanism of the structural evolution in the alkaline HER process to pave a new avenue guiding the design of durable and efficient catalysts.

Received 19th October 2021
Accepted 14th December 2021

DOI: 10.1039/d1ta09010k

rsc.li/materials-a

Published on 15 December 2021. Downloaded on 3/7/2022 5:58:32 AM.

Introduction

Controllable *in situ* structural reconstruction has recently been demonstrated as an effective strategy to optimize activity and stability for alkaline electrocatalytic oxygen evolution reaction (OER).[1] Most transition metal-based electrocatalysts undergo dynamic changes in alkaline media under external electric potential stimuli, such as forming oxide or hydroxide layers, thus influencing the catalytic performance.[2,3] However, the changes and effects of reconstructed species during the alkaline HER process have not yet been investigated. For instance, ABO_4-type oxides, such as molybdates (*e.g.*, $NiMoO_4$ and $CoMoO_4$) and their derived alloys, have been extensively studied as model HER catalysts due to their tunable morphology and composition. We noticed that leaching and transformation of Mo species in the above precatalyst under alkaline HER conditions might induce a surface structural reconstruction, which leads to improved activity.[4,5] Inspired by OER reconstruction strategies, manipulating Mo species through reconstruction is anticipated to be a feasible way to optimize precatalysts by reducing the kinetic energy barrier for efficient and stable alkaline HER performance.

Nevertheless, Mo species' exact reconstruction evolution pathways and their specific contribution are still unidentified, limiting the understanding of the structure–activity relationship to further guide the robust electrocatalyst design in alkaline media. The uppermost obstacle is that the investigation of surface species reconstruction is generally accompanied by distinct changes in the morphology with the interfacial effect,[6,7] which exhibits a detrimental deviation in determining the overarching contribution in electrocatalytic processes. Moreover, the direct reconstruction with the dissolved substrate rather than forming a surface deposition layer with the interfacial effect is less explored. Therefore, it is desirable but challenging to establish a stable micro-environment for in-depth investigation of the surface reconstruction evolution towards realizing the superior alkaline HER performance.

In this work, as a proof of concept, we first develop a hierarchical paradigmatic precatalyst Co@NCNT/$CoMoO_x$ *via* facile acetonitrile liquid-assisted chemical vapor deposition, where

[a]Department of Materials Science and Engineering, City University of Hong Kong, Hong Kong SAR 999077, China. E-mail: johnnyho@cityu.edu.hk
[b]Institute for Materials Chemistry and Engineering, Kyushu University, Fukuoka 816-8580, Japan
[c]Key Laboratory of Advanced Materials Processing & Mold (Zhengzhou University), Ministry of Education, Zhengzhou 450002, China
[d]State Key Laboratory of Terahertz and Millimeter Waves City University of Hong Kong, Hong Kong SAR 999077, China

† Electronic supplementary information (ESI) available. See DOI: 10.1039/d1ta09010k

Published on 15 December 2021. Downloaded on 3/7/2022 5:58:32 AM.

the precatalyst is composed of defective $CoMoO_x$ nanosheets grafted with flexible Co@NCNT arrays as a durable microenvironment. Subsequently, an *in situ* anodic oxidation (AO) reaction is delicately applied to the precatalyst to induce fast and deep MoO_4^{2-} dissolution without discernible morphological changes. The resultant Co@NCNT/$CoMo_yO_x$ system exhibits a significantly superior alkaline HER performance, delivering overpotentials of 94 and 195 mV to reach current densities of −10 and −100 mA cm^{-2}, respectively, and exhibiting excellent stability under a constant 600 h operation in alkaline (sea)water. *In situ* Raman spectroscopy reveals the local high-resolution self-reconstruction of Co@NCNT/$CoMo_yO_x$ with dissolved MoO_4^{2-} in the alkaline HER process, during which the vicinal MoO_4^{2-} is redeposited, then polymerized into $Mo_2O_7^{2-}$, and finally reduced to the Mo–Mo species on the surface of the parent catalyst. The theoretical calculation results further demonstrate that the MoO_4^{2-} self-construction evolution can ultimately provide efficient active sites (Mo–Mo species) for facilitating the kinetics of water adsorption, dissociation, and concomitant hydrogen generation in alkaline media, well rationalizing the experimental reactivity. This work establishes a fundamental understanding of the mechanism associated with the deep self-reconstruction of heterogeneous catalysts toward efficient and stable alkaline HER applications and beyond.

Results and discussion

Material design

The hierarchical Co@NCNT/$CoMoO_x$ heterostructure is synthesized based on a facile two-step reaction: First, the $CoMoO_4$ nanosheet arrays are *in situ* grown on carbon fiber paper (CFP) by a hydrothermal reaction, followed by a thermal treatment in an acetonitrile atmosphere (Fig. 1a and S1†).

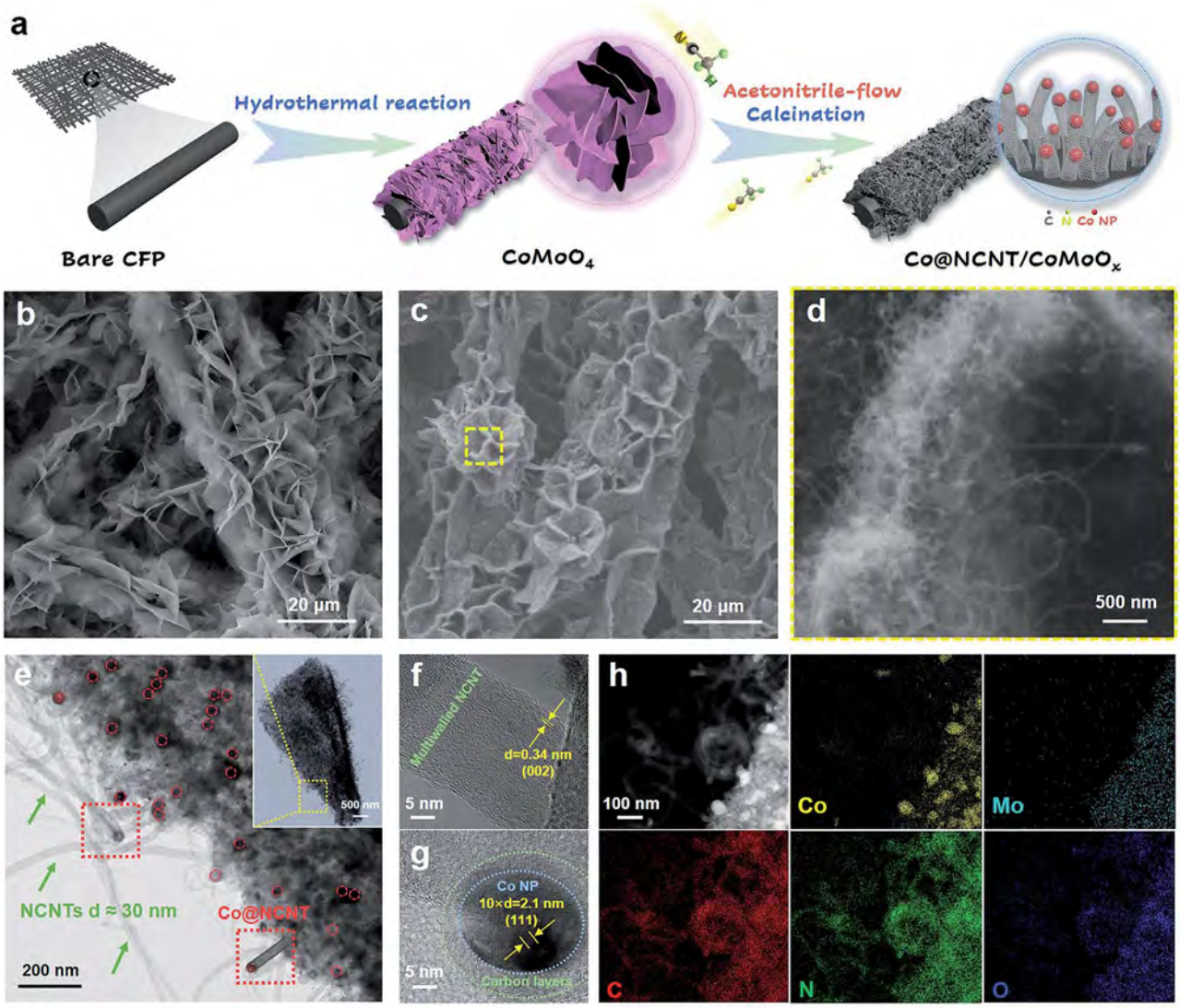

Fig. 1 (a) Schematic illustration of the fabrication process of the Co@NCNT/$CoMoO_x$ precatalyst. SEM images of (b) $CoMoO_4$ and (c, d) Co@NCNT/$CoMoO_x$. (e) TEM image of Co@NCNT/$CoMoO_x$. HRTEM images of (f) NCNT and (g) Co NP. (h) HAADF-STEM image and the elemental mapping image of Co@NCNT/$CoMoO_x$.

 This journal is © The Royal Society of Chemistry 2022

Published on 15 December 2021. Downloaded on 3/7/2022 5:58:32 AM.

During the carbothermal reduction process, acetonitrile is decomposed into hydrogen cyanide (HCN) and methane (CH_4) species, which act as nitrogenous and carbonaceous feedstock to form N-doped carbon nanotubes (NCNTs). Simultaneously, the Co atoms from the $CoMoO_4$ nanosheets undergo outward diffusion to form fine Co metal nanoparticles (NPs) under a reducing atmosphere, serving as catalytic seeds for the tip growth of NCNTs. This way, the $CoMoO_4$ template is transformed into porous amorphous $CoMoO_x$ nanosheets[8] while the NCNTs with their apical domains encapsulating Co NPs are radially grown following the "tip-growth" mechanism.[9] This liquid-assisted chemical vapor deposition is distinctly different from the traditional H_2/Ar calcination for the growth of CNTs.[10,11]

The typical diffraction patterns belonging to $CoMoO_4$ are discerned along with the peaks of CFP (Fig. S2a†).[12] Meanwhile, the optical color of the CFP substrate turns from gray to pink, indicating the uniform growth of $CoMoO_4$ (Fig. S2b†). Scanning electron microscopy (SEM) shows that the $CoMoO_4$ nanosheets with smooth surfaces are vertically aligned on the conductive CFP (Fig. 1b). The transmission electron microscopy (TEM) and high-resolution TEM (HRTEM) images depict that the $CoMoO_4$ nanosheet features with a thin-layered structure, wherein the lattice fringe with an interplanar spacing of 0.26 nm can be assigned to the (−222) plane (Fig. S3†). The high-angle annular dark-field scanning TEM (HAADF-STEM) and corresponding elemental mapping images demonstrate the homogeneous distributions of Co, Mo, and O elements within the $CoMoO_4$ nanosheets (Fig. S4†). Energy-dispersive X-ray spectroscopy (EDS) and X-ray photoelectron spectroscopy (XPS) images further validate the coexistence of Co, Mo, and O elements (Fig. S5 and S6†).[13,14] In addition, the relatively high atomic ratio of Co/Mo may result from the existence of separate amorphous Co oxides underneath the surface of $CoMoO_4$ species, as revealed by the corresponding Raman spectrum (Fig. S7†).

As depicted in Fig. 1c, the overview SEM image of Co@NCNT/$CoMoO_x$ exhibits a well-maintained nanosheet-array structure with a rough surface after the acetonitrile-assisted carbothermal reduction reaction. The magnified SEM images delineate that the nanosheet skeleton is covered by numerous NCNTs with high flexibility (Fig. 1d). A typical TEM image displays that the Co NPs are encapsulated at the tip of NCNTs, which exhibit an average diameter of 30 nm (Fig. 1e). Moreover, it is observed from the HRTEM image that the NCNT is multi-walled with a lattice fringe of 0.34 nm (Fig. 1f), corresponding to the (002) plane of graphitic carbon.[15] Meanwhile, a well-resolved lattice fringe of 0.21 nm is detected in the apical particle, which can be indexed to the (111) lattice plane of the metallic Co phase (Fig. 1g).[16] In addition, Co@NCNT/$CoMoO_x$ shows distinctive diffraction peaks of metallic Co crystals and carbon, further affirming the formation of Co NPs and NCNTs (Fig. S8†).[17] Notably, it is assumed that the 2D $CoMoO_4$ backbone is transformed into an amorphous state (denoted as $CoMoO_x$) owing to the outward diffusion of the Co element and deoxidation (Fig. S9†). The HRTEM images highlight that the structure of the sheet-backbone in Co@NCNT/$CoMoO_x$ features a long-range disorder and a short-range order with rich defects (Fig. S10†).[18,19] Also, the corresponding HAADF-STEM image and elemental mapping image display that the N and C elements are uniformly distributed across the whole heterostructure shown in Fig. 1h, indicating the formation of NCNT sub-arrays. An intensive distribution of Co elements demonstrates the exsolved Co NPs.[20] Besides, the Co, Mo, and O elements are homogeneously dispersed on the sheet structure, which attests to the formation of $CoMoO_x$ sheets.

The time-dependent control experiments are conducted to unravel the growth mechanism (Fig. S11†). It is found that the Co NPs are exsolved on the sheet-platform surface at the beginning. The NCNTs are next orientally grown with Co NPs at the tip and their length is elongated with the increasing growth time. These observations elucidate that the Co NPs derived from $CoMoO_4$ nanosheets can *in situ* catalyze the growth of high-quality NCNTs by the "tip-growth" mechanism in an acetonitrile atmosphere, forming a 2D amorphous $CoMoO_x$ backbone. In addition, the powder sample is prepared by an identical two-step synthesis process without using CFP as a substrate. The XRD pattern of Co@NCNT/$CoMoO_x$ powder under no CFP influence is found to exhibit the diffraction peaks of metallic Co and carbon without the distinct peaks of $CoMoO_x$, further indicating the formation of amorphous $CoMoO_x$ and the generation of Co@NCNTs by the acetonitrile-assisted carbothermal reduction reaction (Fig. S12†). The corresponding SEM images show that the freestanding $CoMoO_x$ backbone material is covered by intertwined Co@NCNTs, accompanying severe agglomeration and structural collapse (Fig. S13†). These findings prove the structural stability and advantage of the self-supported nanosheet arrays synthesized directly on CFP. As a comparative experiment, the CoO counterpart precursor shaped as interconnected octahedra is unevenly grown on CFP by an identical hydrothermal reaction without feeding the Mo source and then calcined in an acetonitrile atmosphere. The resulting product is observed to generate uneven-sized Co@NCNTs with diameters ranging from 50 to 200 nm (Fig. S14†). It is due to the fact that the $CoMoO_4$ nanosheet arrays as 3D porous structures avail the diffusion and contact of acetonitrile molecules to form fine Co NPs and also uniform Co@NCNT sub-arrays. Therefore, it is worth mentioning that the as-obtained 3D heterostructure exhibits multi-level porosities and open channels, which are in favor of the effective solution permeability and gas release for electrocatalytic reactions.[21] The as-obtained Co@NCNT sub-arrays can act as a physical buffer to strengthen the robustness of the entire heterostructure, which is beneficial for the subsequent exploration of dissolution and self-reconstruction mechanisms with structural integrity.

Alkaline HER performance

In the following, the electrocatalytic HER performance of Co@NCNT/$CoMoO_x$ is evaluated in 1.0 M KOH by using a standard three-electrode system. An *in situ* AO reaction for rapid MoO_4^{2-} dissolution as a pre-treatment is applied on Co@NCNT/$CoMoO_x$. The as-obtained sample is denoted as Co@NCNT/$CoMo_yO_x$. As shown in Fig. 2a, the polarization

Published on 15 December 2021. Downloaded on 3/7/2022 5:58:32 AM.

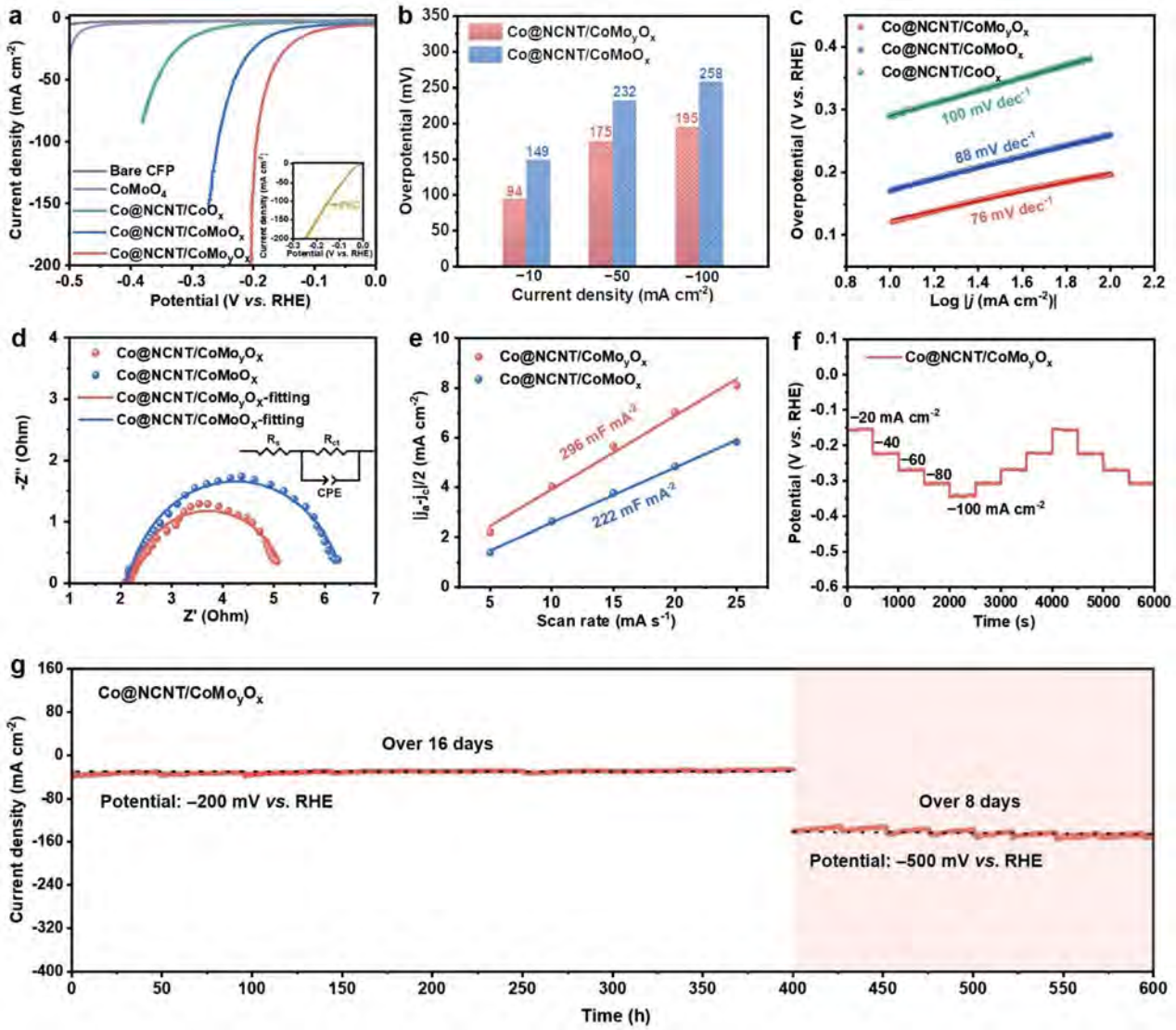

Fig. 2 HER performance in 1.0 M KOH solution. (a) Polarization curves (inset: benchmark Pt/C). (b) Overpotential comparison. (c) The corresponding Tafel plots derived from the polarization curves in (a). (d) Nyquist plots recorded at −0.19 V *vs.* RHE (inset: equivalent circuit model). (e) The C_{dl} values. (f) Multicurrent step CP curve and (g) CA curve without iR correction.

curves reveal that the performance of Co@NCNT/$CoMo_yO_x$ is significantly improved as compared with that of the pristine Co@NCNT/$CoMoO_x$, Co@NCNT/CoO_x counterpart, and $CoMoO_4$ for alkaline HER. Specifically, the obtained Co@NCNT/$CoMo_yO_x$ sample requires 94, 175, and 195 mV to reach current densities of −10, −50, and −100 mA cm^{-2}, respectively, while the overpotentials of 149, 232, and 258 mV are needed for Co@NCNT/$CoMoO_x$ precatalysts to achieve the same current densities, accordingly (Fig. 2b). Since Co@NCNT/$CoMo_yO_x$ is a noble metal-free material, the HER activity is slightly inferior to that of Pt/C (35 mV at −10 mA cm^{-2}) in the alkaline electrolyte (Fig. 2a, inset). Meanwhile, the alkaline HER performance of Co@NCNT/$CoMo_yO_x$ is superior to that of most reported carbon/transition metal-based materials (Table S1†). Besides, the Tafel slope of Co@NCNT/$CoMo_yO_x$ exhibits the lowest value of 76 mV dec^{-1} as compared with those of Co@NCNT/$CoMoO_x$ precatalysts (88 mV dec^{-1}) and Co@NCNT/CoO_x counterparts (100 mV dec^{-1}), indicating the superior kinetics of Co@NCNT/$CoMo_yO_x$ determined by the Volmer–Heyrovsky process (Fig. 2c).[22] These results disclose the promoting effect of MoO_4^{2-} dissolution engineering on alkaline HER performance. In addition, after submitting $CoMoO_4$ directly to the identical AO treatment, the obtained sample exhibits a slightly improved HER performance compared to the pristine $CoMoO_4$ (Fig. S15†). This result can be ascribed to two important impacts of acetonitrile calcination. (i) The acetonitrile calcination can induce outward diffusion of Co from $CoMoO_4$ to form the amorphous $CoMoO_x$ nanosheets with abundant defects in Co@NCNT/$CoMoO_x$. In this way, the pristine $CoMoO_4$ is more stable than the amorphous $CoMoO_x$ of Co@NCNT/$CoMoO_x$ so that MoO_4^{2-} in $CoMoO_4$ is harder to dissolve into the solution and then experiences self-

 This journal is © The Royal Society of Chemistry 2022

Published on 15 December 2021. Downloaded on 3/7/2022 5:58:32 AM.

construction. (ii) The Co@NCNT sub-arrays grown through acetonitrile calcination create an essential stable micro-environment for Co@NCNT/$CoMoO_x$ to reach quasi-equilibrium for self-construction evolution.

Furthermore, the electrochemical impedance spectroscopy (EIS) analysis and double-layer capacitance (C_{dl}) measurement are performed on Co@NCNT/$CoMoO_x$ and Co@NCNT/$CoMo_yO_x$ to elucidate the merits of MoO_4^{2-} dissolution engineering. The Nyquist plots reveal that Co@NCNT/$CoMo_yO_x$ exhibits a lower charge transfer resistance (3.10 Ω) than that of Co@NCNT/$CoMoO_x$ (4.26 Ω), implying a better charge-transfer capacity for Co@NCNT/$CoMo_yO_x$ (Fig. 2d, Table S2†). The C_{dl} value of Co@NCNT/$CoMo_yO_x$ is found to be 296 mF cm^{-2}, larger than that of Co@NCNT/$CoMoO_x$ (222 mF cm^{-2}) (Fig. 2e and S16†).[23] It is suggested that the number of catalytically active sites is increased on the sample after the *in situ* AO reaction for MoO_4^{2-} dissolution.[24]

The multistep chronopotentiometry (CP) curve of Co@NCNT/$CoMo_yO_x$ is recorded as the current density increases stepwise from −20 to −100 mA cm^{-2} (Fig. 2f). Each step lasts for a duration of 500 s, showing the instantly stable state as the current changes and verifying the excellent ion/mass transport and mechanical robustness of the Co@NCNT/$CoMo_yO_x$ sample.[2] To further study its stability for H_2 generation with prolonged time, Fig. 2g shows the longevity of the Co@NCNT/$CoMo_yO_x$ sample on continuous chronoamperometry (CA) operation for 600 h in alkaline solution, including 400 h and 200 h tests at fixed potentials of −200 mV and −500 mV *vs.* RHE, respectively.[25] Consequently, the catalyst exhibits outstanding long-term stability with a negligible fluctuation at constant current densities on the four-week timescale.

Mechanism exploration

To investigate the underlying mechanism for enhanced activity and stability, systematic structural characterization of the Co@NCNT/$CoMoO_x$ sample before and after the fast AO treatment is carried out. Co@NCNT/$CoMo_yO_x$ sustains the

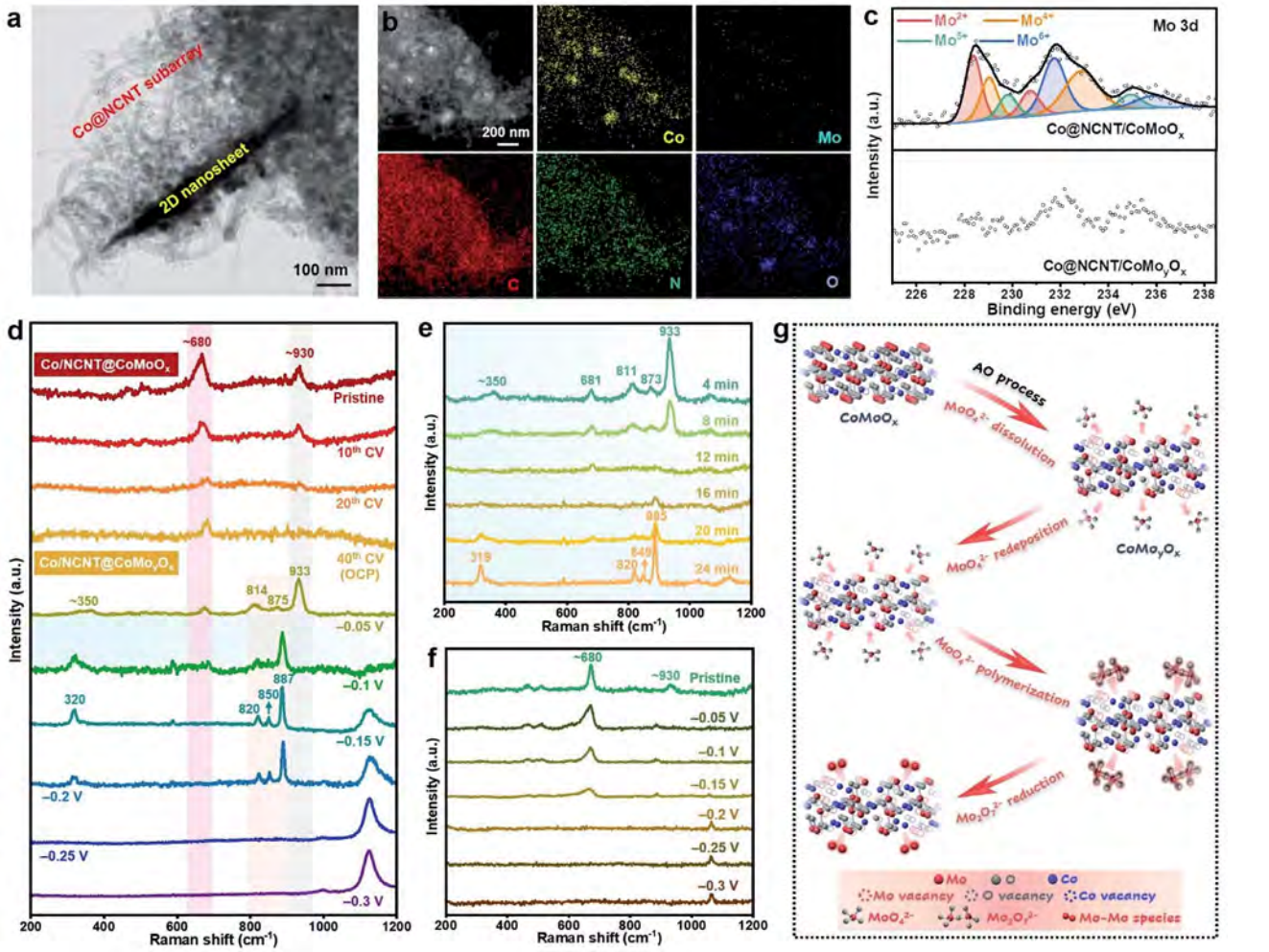

Fig. 3 Mechanism exploration. (a) TEM image and (b) HAADF-STEM image and elemental mapping image of Co@NCNT/$CoMo_yO_x$. (c) High-resolution XPS spectrum of Mo 3d. (d) *In situ* Raman spectra of the AO process and potential-dependent tests (*vs.* RHE). (e) Time-dependent *in situ* Raman spectra at −0.1 V *vs.* RHE of Co@NCNT/$CoMo_yO_x$. (f) Potential-dependent *in situ* Raman spectra of Co@NCNT/$CoMoO_x$. (g) Schematic illustration of the self-reconstruction evolution pathways.

Published on 15 December 2021. Downloaded on 3/7/2022 5:58:32 AM.

hierarchical heterostructure well, which includes the nanosheet arrays assembled with flexible Co@NCNT sub-arrays, implying the stability of the 3D multi-level porous heterostructure (Fig. 3a and S17†). As compared with the Co@NCNT/$CoMoO_x$ pre-catalyst, a distinct decrease of the Mo element occurs in Co@NCNT/$CoMo_yO_x$ as revealed by the elemental mapping image, confirming the dissolution of Mo species into the alkaline solution (Fig. 3b).[3] Also, the comparison of EDS images demonstrates that the Mo/Co atomic ratios are significantly decreased after the AO treatment (Fig. S18†). These changes in the chemical composition and valence state of the samples are further investigated through XPS analysis.[26] For pristine Co@NCNT/$CoMoO_x$, the Mo 3d spectrum exhibits four characteristic states, corresponding to Mo^{2+} (228.4 and 230.7 eV), Mo^{4+} (229.0 and 232.9 eV), Mo^{5+} (229.8 and 234.9 eV), and Mo^{6+} (231.7 and 235.9 eV), respectively (Fig. 3c).[27–29] In contrast, the weak Mo^{6+} signals are detected from the Mo 3d spectrum of Co@NCNT/$CoMo_yO_x$,[30] suggesting that a large amount of Mo species is oxidized and dissolved into the electrolyte in the form of MoO_4^{2-},[31] which is consistent with the mapping and EDS results. Besides, the Co 2p spectrum of Co@NCNT/$CoMo_yO_x$ shows a slight increase in the peak area ratio of Co^{3+}/Co^{2+} as compared with that of pristine Co@NCNT/$CoMoO_x$, which could be ascribed to the re-formation of cobalt oxides after the dissolution of MoO_4^{2-} in the $CoMoO_x$ matrix (Fig. S19a†).[32] Simultaneously, the metallic state (Co^0) corresponding to the Co NPs is still present, benefiting from the tight encapsulation of the carbon layers that protect the inner Co NPs from corrosion.[29] As shown in Fig. S19b,† there are three typical XPS peaks of O 1s, which are attributed to the lattice oxygen, defect sites of oxygen, and absorbed water molecules on the surface, respectively.[33] The larger peak area of defect sites of oxygen in Co@NCNT/$CoMo_yO_x$ than that in the precatalyst indicates the presence of much more oxygen vacancies owing to the MoO_4^{2-} dissolution. Moreover, the N 1s spectrum of Co@NCNT/$CoMoO_x$ exhibits three peaks assigned to pyridinic N, pyrrolic N, and oxidized N, while the C 1s spectrum shows the peaks ascribed to C=C/C–C, C–N, C–O, and O–C=O (Fig. S19c, d†).[34,35] All these peaks only exhibit slight shifts in N 1s and C 1s spectra of Co@NCNT/$CoMo_yO_x$, implying the robustness of Co@NCNT sub-arrays with a negligible influence during the AO reaction.

Even after the long-term stability test for 600 h, the 2D nanosheet backbone is well maintained and covered with numerous 1D Co@NCNTs sub-units in Co@NCNT/$CoMo_yO_x$ (Fig. S20†). In addition, the survey and high-resolution XPS spectra show the coexistence of Co (Co^{3+}, Co^{2+}, and Co^0), O, N, and C elements and weak signal of the Mo element (Fig. S21 and S22†). In principle, the stable hierarchical 3D heterostructure with different porosity levels contributes to rapid gaseous product release, eliminating the structural destruction from bubble accumulation.[36] Moreover, the *in situ* growth of flexible Co@NCNT sub-arrays firmly covers the surface of $CoMoO_x$ nanosheet arrays, which act as a physical buffer to strengthen the structural integrity.[37] On the other hand, the robust Co@NCNT sub-network can facilitate efficient electron transfer by improving the conductivity while the amorphous $CoMo_yO_x$ nanosheets provide abundant active sites for H_2 generation, thus promoting alkaline HER efficiency.[38]

In situ Raman spectroelectrochemistry

To elucidate the effect of dissolution and reconstruction processes on HER performance, we employ *in situ* Raman spectroelectrochemistry with constant cycles and controlled potentials under identical reaction conditions. For the pristine Co@NCNT/$CoMoO_x$, the distinctive bands located at around 680 and 930 cm^{-1} are associated with the symmetric stretching of the Co–O–Mo and Mo=O bonds, respectively (Fig. 3d).[39] It is observed that the intensities of Co–O–Mo and Mo=O bonds are accordingly reduced as the AO reaction proceeds, revealing the corresponding bond cleavages ascribed to MoO_4^{2-} etching from the $CoMoO_x$ matrix.[40] After the final 40th CV cycle, the Mo=O bond is undetectable, suggesting the fast and large leaching of MoO_4^{2-} from Co@NCNT/$CoMoO_x$.

Subsequently, a negative potential is applied on Co@NCNT/$CoMo_yO_x$ with a magnitude of −0.05 V. As a result, the new bands located at 814, 875, and 933 cm^{-1} and a broad-band at ~350 cm^{-1} appear at a potential of −0.05 V *vs.* RHE, which can be indexed to the MoO_4^{2-} species.[41] Specifically, the mode located at 350 cm^{-1} corresponds to asymmetric and symmetric bending modes of O–Mo–O; and the bands at 814 and 875 cm^{-1} are related to asymmetric stretching modes of oxygen in binding O–Mo–O. The strongest band at 933 cm^{-1} can be attributed to the symmetric stretching mode of Mo=O. This way, the dissolved MoO_4^{2-} species gets redeposited onto the surface of the parent material at the initial stage of the HER process. When decreased to −0.1 V, the new bands become noisy, indicating the evolution of new species on the surface. Next, at more negative potentials of −0.15 and −0.2 V *vs.* RHE, the distinctive bands at 320, 820, 850, and 887 cm^{-1} are detected, which can be ascribed to the Mo–O vibration modes of the $Mo_2O_7^{2-}$ species.[42] This $Mo_2O_7^{2-}$ signal indicates that the polymerization happens in the newly redeposited MoO_4^{2-}. Besides, a broad-band at around 1120 cm^{-1} appeared at −0.15 and −0.2 V *vs.* RHE, which is the second-order Raman scattering from optical modes in CoO.[43] This phenomenon records the reconstruction of Co–O in the matrix of $CoMoO_x$ because of the large number of bond cleavages induced by the MoO_4^{2-} etching. Afterward, time-dependent *in situ* Raman spectroelectrochemistry is performed to track the details of surface structural reconstruction at −0.1 V *vs.* RHE. As shown in Fig. 3e, the initial well-defined Raman peaks at ~350, 681, 811, 873, and 933 cm^{-1} are ascribed to the redeposition of dissolved MoO_4^{2-} on the surface of Co@NCNT/$CoMo_yO_x$. These peaks are weakened and disappear in the next 12 min. Subsequently, new peaks at 319, 820, 849, and 885 cm^{-1} appear and are strengthened, recording the process that the redeposited MoO_4^{2-} evolves into the polymerized $Mo_2O_7^{2-}$ species. Simultaneously, the band at ~1120 cm^{-1} also arises for the reconstruction of Co–O. The traced dynamic evolution at −0.1 V *vs.* RHE is well consistent with the potential-dependent *in situ* Raman results. As the negative potential is below −0.2 *vs.* RHE (Fig. 3d), only one distinctive band located at 1120 cm^{-1} is detected,

 This journal is © The Royal Society of Chemistry 2022

Published on 15 December 2021. Downloaded on 3/7/2022 5:58:32 AM.

suggesting that the polymerized $Mo_2O_7^{2-}$ species are reduced into the Mo–Mo species on the surface based on the Pourbaix diagram (Fig. S23†). As a control experiment, the obtained Co@NCNT/$CoMo_yO_x$ is carefully washed with DI water and the electrolyte is replaced to controllably create the conditions corresponding to no dissolved Mo species in the solution. It is found that the washed sample exhibits only a somewhat decreased HER performance (Fig. S24†). In this way, the assumption of the complete dissolution of surface Mo species with the disappearance of the $Mo_2O_7^{2-}$ signals can be excluded.

To explicitly interrogate the role of MoO_4^{2-} dissolution engineering, the pristine Co@NCNT/$CoMoO_x$ precatalyst is directly employed to the potential-dependent *in situ* Raman spectroelectrochemistry without AO treatment for comparison. As can be observed from Fig. 3f, the peaks at ~680 and ~930 cm^{-1} gradually disappear in the potential range from −0.05 to −0.2 V *vs.* RHE. The new peak of reconstructed Co–O appears from −0.2 to −0.3 V *vs.* RHE, manifesting that MoO_4^{2-} is slowly dissolved from the Co@NCNT/$CoMoO_x$ precatalyst because the spontaneous dissolution rate in the alkaline media is still faster than the electrochemical deposition and conversion rate. Meanwhile, compared with the AO-pretreated sample, the slight blueshift of the Co–O peak could result from the discrepancy of strain effects and/or defects induced by the different reconstruction processes of Mo species.[44] On the other hand, it is demonstrated that the elaborated MoO_4^{2-} dissolution engineering is a helpful and efficient method to obtain the electrocatalyst without unstable MoO_4^{2-} etching and thus creating the possibility for tracing its following evolution. Moreover, we analyze the content of Mo and Co in the electrolyte by using inductively coupled plasma-mass spectrometry (ICP-MS). By the CA test, it is shown that the content of Co remains at a low level throughout the process. In contrast, the content of Mo continuously increases with prolonged time (Fig. S25†). The ICP-MS analysis results further confirm the component instability of Co@NCNT/$CoMoO_x$ with MoO_4^{2-} dissolution in the alkaline media, which agrees well with the above findings from the *in situ* Raman results. Comparatively, the Mo content distinctly increases in the electrolyte after the AO reaction to prepare Co@NCNT/$CoMo_yO_x$ and then it remains almost unchanged under subsequent HER activity (Fig. S26†), indicating that fast MoO_4^{2-} dissolution purposely occurs and then a quasi-equilibrium of self-construction evolution is attained to maintain the steady Mo content in the electrolyte (Fig. 3g). Furthermore, the EDS analysis of the corresponding post-HER Co@NCNT/$CoMo_yO_x$ sample exhibits a very similar Mo/Co atomic ratio to that of pristine Co@NCNT/$CoMo_yO_x$ (Fig. S27 and S18†), consistent with the ICP result. The dynamic equilibria of redeposition, polymerization, and reduction evolution on the surface promote the formation of active species and maximize the component utilization, improving the efficiency of alkaline HER activity with long-term stability.[21]

Theoretical calculations

To further identify the origin of active sites, density functional theory (DFT) calculations are carried out to simulate the elementary steps of alkaline HER.[30] $CoMo_yO_x$ adsorbed with the ultimate Mo–Mo species (denoted as $CoMo_yO_x$(Mo–Mo)) is investigated while the $CoMoO_x$ and $CoMo_yO_x$ are applied as comparative models (Fig. 4a, insets). It should be noted that the proposed $CoMo_yO_x$(Mo–Mo) structural model is simplified for the interpretation of the structure–activity relationship, which needs further investigations. As shown in Fig. 4a, the calculated H_2O adsorption free energies for $CoMoO_x$, $CoMo_yO_x$, and $CoMo_yO_x$(Mo–Mo) are −0.525, −0.376, and −0.918 eV, respectively. It is demonstrated that the water adsorption on $CoMo_yO_x$ is weaker than that on $CoMoO_x$ owing to the MoO_4^{2-} dissolution. Furthermore, after the subsequent MoO_4^{2-} evolution process, the ultimate $CoMo_yO_x$(Mo–Mo) state has the strongest water adsorption ability, manifesting the fact that the evolved Mo–Mo species on the surface of $CoMo_yO_x$ can prominently

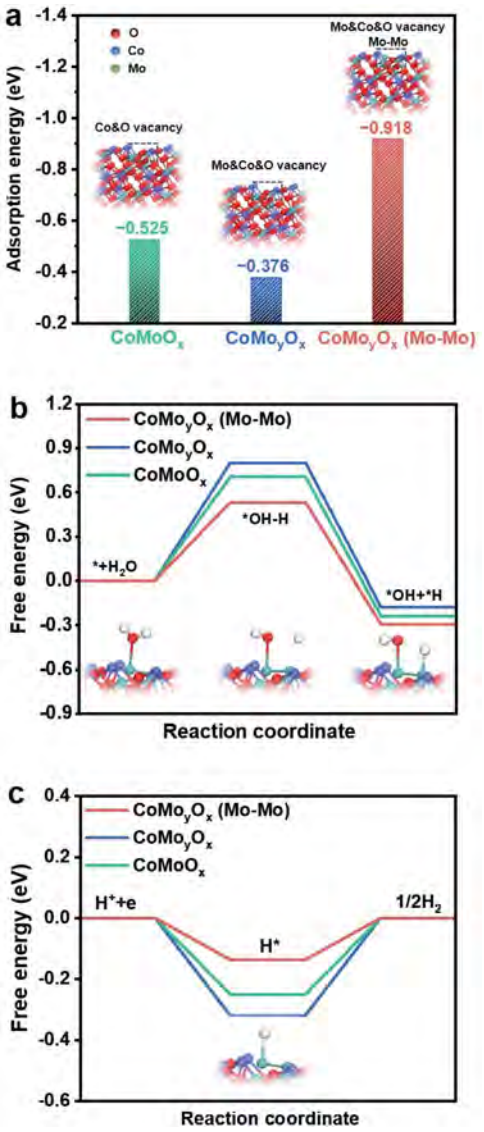

Fig. 4 DFT calculations. Free energy diagrams of (a) water adsorption, (b) water dissociation, and (c) hydrogen adsorption (inset of (a): the structural models of $CoMoO_x$, $CoMo_yO_x$, and $CoMo_yO_x$(Mo–Mo); insets of (b) and (c): the atomic configurations of different states of $CoMo_yO_x$ (Mo–Mo)).

Published on 15 December 2021. Downloaded on 3/7/2022 5:58:32 AM.

contribute to forming the initial catalyst-H_2O state in order to accelerate the alkaline HER kinetics.[45] Besides, compared with $CoMoO_x$ and $CoMo_yO_x$, $CoMo_yO_x$(Mo–Mo) has the lowest energy barrier for the water dissociation (ΔG_{H_2O}), revealing that the step in which adsorbed H_2O generates a proton in alkaline media is facilitated on the surface of ultimate $CoMo_yO_x$(Mo–Mo) (Volmer step) (Fig. 4b and S28†).[46] Meanwhile, as observed from Fig. 4c, $CoMo_yO_x$ (Mo–Mo) features the smallest hydrogen binding free energy ($|\Delta G_{H^*}| = 0.137$ eV), illustrating an optimal balance between the adsorption and desorption processes for promoting the subsequent hydrogen evolution step (Heyrovsky step) (Fig. S29†). The increased $|\Delta G_{H^*}|$ for $CoMoO_x$ and $CoMo_yO_x$ means a suppressed desorption of atomic hydrogen with the active sites blocked, hindering H_2 generation.[47,48] These theoretical calculation results corroborate that the MoO_4^{2-} self-construction process can ultimately provide efficient active sites (Mo–Mo species) for facilitating the kinetics of water adsorption, dissociation, and concomitant hydrogen generation in alkaline media, well rationalizing the experimental reactivity.

Application in natural seawater

For practical applications, the HER activity of samples is recorded in alkaline seawater (Table S3†).[49] $Co@NCNT/CoMo_yO_x$ exhibits an obvious improvement of HER activity as compared with that of the $Co@NCNT/CoMoO_x$ precatalyst in natural alkaline seawater (Fig. 5a). Specifically, $Co@NCNT/CoMo_yO_x$ requires an overpotential of 125 mV at a current density of -10 mA cm^{-2}, which is superior to that of $Co@NCNT/CoMoO_x$ (198 mV) (Fig. 5b). Likewise, to reach the high current densities of -100 and -200 mA cm^{-2} in alkaline seawater, $Co@NCNT/CoMo_yO_x$ delivers smaller overpotentials of 259 and 288 mV, respectively, as compared with those of the $Co@NCNT/CoMoO_x$ precatalyst (297 and 342 mV). Such performance in natural seawater is also better than that of most reported transition-metal-based materials (Table S4†). These results demonstrate that the MoO_4^{2-} dissolution engineering and the following reconstruction evolution positively contribute to facilitating electrocatalytic H_2 generation in a high salinity environment.[50] Moreover, the long-term durability of catalysts in seawater is another important metric. Notably, $Co@NCNT/CoMo_yO_x$ shows excellent stability at -10 mA cm^{-2} for 400 h and then at a high current density of -100 mA cm^{-2} for 200 h without any noticeable degradation in the alkaline seawater (Fig. 5c).[49] The corrosion-resistant robustness of $Co@NCNT/CoMo_yO_x$ can be ascribed to the fact that the multilevel-porous heterostructure is under the protection of the flexible NCNT sub-network. These results not only indicate the superior durability under harsh conditions for the catalyst after MoO_4^{2-} dissolution engineering but also demonstrate its feasibility in efficient seawater splitting applications.[51]

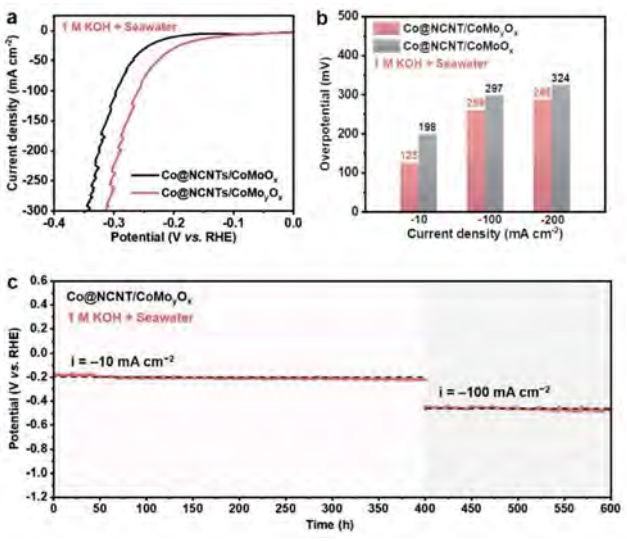

Fig. 5 HER performance in natural alkaline seawater. (a) Polarization curves. (b) Overpotential comparison. (c) CP curve without iR correction.

Conclusions

In summary, we synthesize a hierarchical precatalyst and harness the MoO_4^{2-} reconstruction evolution toward a durable and efficient alkaline HER activity. $Co@NCNT/CoMoO_x$ is constituted with $CoMoO_x$ nanosheet arrays assembled with flexible Co@NCNT sub-arrays, which serve as a physical buffer to maintain structural integrity. Then, fast and deep MoO_4^{2-} dissolution is triggered on the precatalyst *via* an *in situ* AO reaction to obtain $Co@NCNT/CoMo_yO_x$. As a result, $Co@NCNT/CoMo_yO_x$ exhibits a significantly improved alkaline HER performance as compared with that of the precatalyst. Moreover, $Co@NCNT/CoMo_yO_x$ exhibits decent stability for H_2 evolution under a constant 600 h operation in both alkaline freshwater and seawater. *In situ* Raman spectroscopy sophisticatedly traces the evolution process that the dissolved MoO_4^{2-} is redeposited, then polymerized into the $Mo_2O_7^{2-}$ species, and finally reduced to the Mo–Mo species on the surface of the parent material. The DFT calculations indicate that the final Mo–Mo species acting as efficient active sites can facilitate the water adsorption, dissolution and thus significantly enhance the alkaline HER activity. Our work could provide a reference for adsorption-modulated electrocatalysts toward other reduction reactions, such as the oxygen reduction reaction, CO_2 reduction reaction, and aqueous organic hydrogenation reaction.

Conflicts of interest

There are no conflicts to declare.

Acknowledgements

This work was financially supported by the Environment and Conservation Fund of Hong Kong SAR, China (ECF 2020-13), the Theme-based Research Scheme (T42-103/16-N) of the Research Grants Council of Hong Kong SAR, China, the City University of Hong Kong (project no. 9667227), and the Foshan Innovative and Entrepreneurial Research Team Program (No. 2018IT100031).

 This journal is © The Royal Society of Chemistry 2022

Published on 15 December 2021. Downloaded on 3/7/2022 5:58:32 AM.

References

1 F.-Y. Chen, Z.-Y. Wu, Z. Adler and H. Wang, *Joule*, 2021, **5**, 1704–1731.
2 Y. Wang, Y. Zhu, S. Zhao, S. She, F. Zhang, Y. Chen, T. Williams, T. Gengenbach, L. Zu, H. Mao, W. Zhou, Z. Shao, H. Wang, J. Tang, D. Zhao and C. Selomulya, *Matter*, 2020, **3**, 2124–2137.
3 F. Cheng, Z. Li, L. Wang, B. Yang, J. Lu, L. Lei, T. Ma and Y. Hou, *Mater. Horiz.*, 2021, **8**, 556–564.
4 J. A. Bau, S. M. Kozlov, L. M. Azofra, S. Ould-Chikh, A.-H. Emwas, H. Idriss, L. Cavallo and K. Takanabe, *ACS Catal.*, 2020, **10**, 12858–12866.
5 J. A. Bau, H. Haspel, S. Ould-Chikh, A. Aguilar-Tapia, J.-L. Hazemann, H. Idriss and K. Takanabe, *J. Mater. Chem. A*, 2019, **7**, 15031–15035.
6 Y. Zhang, L. Gao, E. J. M. Hensen and J. P. Hofmann, *ACS Energy Lett.*, 2018, **3**, 1360–1365.
7 J. Lai, B. Huang, Y. Chao, X. Chen and S. Guo, *Adv. Mater.*, 2019, **31**, 1805541.
8 J. Yu, G. Li, H. Liu, L. Zeng, L. Zhao, J. Jia, M. Zhang, W. Zhou, H. Liu and Y. Hu, *Adv. Sci.*, 2019, **6**, 1901458.
9 W. Niu, S. Pakhira, K. Marcus, Z. Li, J. L. Mendoza-Cortes and Y. Yang, *Adv. Energy Mater.*, 2018, **8**, 1800480.
10 A. Aijaz, J. Masa, C. Rösler, W. Xia, P. Weide, A. J. R. Botz, R. A. Fischer, W. Schuhmann and M. Muhler, *Angew. Chem., Int. Ed.*, 2016, **55**, 4087–4091.
11 W. Gong, Y. Lin, C. Chen, M. Al-Mamun, H.-S. Lu, G. Wang, H. Zhang and H. Zhao, *Adv. Mater.*, 2019, **31**, 1808341.
12 L.-Q. Mai, F. Yang, Y.-L. Zhao, X. Xu, L. Xu and Y.-Z. Luo, *Nat. Commun.*, 2011, **2**, 381.
13 Y. Zhang, Q. Shao, S. Long and X. Huang, *Nano Energy*, 2018, **45**, 448–455.
14 T. Ouyang, X.-T. Wang, X.-Q. Mai, A.-N. Chen, Z.-Y. Tang and Z.-Q. Liu, *Angew. Chem., Int. Ed.*, 2020, **59**, 11948–11957.
15 J. Lin, C. Zeng, X. Lin, C. Xu, X. Xu and Y. Luo, *ACS Nano*, 2021, **15**, 4594–4607.
16 T. Li, G. Luo, K. Liu, X. Li, D. Sun, L. Xu, Y. Li and Y. Tang, *Adv. Funct. Mater.*, 2018, **28**, 1805828.
17 Q. Cheng, S. Han, K. Mao, C. Chen, L. Yang, Z. Zou, M. Gu, Z. Hu and H. Yang, *Nano Energy*, 2018, **52**, 485–493.
18 S. Hong, C. S. Lee, M. H. Lee, Y. Lee, K. Y. Ma, G. Kim, S. I. Yoon, K. Ihm, K. J. Kim, T. J. Shin, S. W. Kim, E. C. Jeon, H. Jeon, J. Y. Kim, H. I. Lee, Z. Lee, A. Antidormi, S. Roche, M. Chhowalla, H. J. Shin and H. S. Shin, *Nature*, 2020, **582**, 511–514.
19 H. Zhou, M. Zheng, H. Tang, B. Xu, Y. Tang and H. Pang, *Small*, 2020, **16**, 1904252.
20 G. Qian, J. Chen, T. Yu, L. Luo and S. Yin, *Nano-Micro Lett.*, 2021, **13**, 77.
21 X. Liu, J. Meng, J. Zhu, M. Huang, B. Wen, R. Guo and L. Mai, *Adv. Mater.*, 2021, **33**, 2007344.
22 C. Lei, Y. Wang, Y. Hou, P. Liu, J. Yang, T. Zhang, X. Zhuang, M. Chen, B. Yang, L. Lei, C. Yuan, M. Qiu and X. Feng, *Energy Environ. Sci.*, 2019, **12**, 149–156.
23 Y. Zhao, H. Cong, P. Li, D. Wu, S. Chen and W. Luo, *Angew. Chem., Int. Ed.*, 2021, **60**, 7013–7017.
24 Q. Quan, T. Zhang, C. Lei, B. Yang, Z. Li, J. Chen, C. Yuan, L. Lei and Y. Hou, *Nanoscale*, 2019, **11**, 22261–22269.
25 C. Ziliang, W. Renbing, L. Yang, H. Yuan, G. Yanhui, S. Dalin, L. Miao and F. Fang, *Adv. Mater.*, 2018, **30**, e1802011.
26 M. Li, Y. Zhu, H. Wang, C. Wang, N. Pinna and X. Lu, *Adv. Energy Mater.*, 2019, **9**, 1803185.
27 M. Zang, N. Xu, G. Cao, Z. Chen, J. Cui, L. Gan, H. Dai, X. Yang and P. Wang, *ACS Catal.*, 2018, **8**, 5062–5069.
28 L. Yu, Y. Xiao, C. Luan, J. Yang, H. Qiao, Y. Wang, X. Zhang, X. Dai, Y. Yang and H. Zhao, *ACS Appl. Mater. Interfaces*, 2019, **11**, 6890–6899.
29 H. Shi, Y.-T. Zhou, R.-Q. Yao, W.-B. Wan, X. Ge, W. Zhang, Z. Wen, X.-Y. Lang, W.-T. Zheng and Q. Jiang, *Nat. Commun.*, 2020, **11**, 2940.
30 M. Wang, H. Yang, J. Shi, Y. Chen, Y. Zhou, L. Wang, S. Di, X. Zhao, J. Zhong, T. Cheng, W. Zhou and Y. Li, *Angew. Chem., Int. Ed.*, 2021, **60**, 5771–5777.
31 J. H. J. Wijten, R. L. Riemersma, J. Gauthier, L. D. B. Mandemaker, M. W. G. M. Verhoeven, J. P. Hofmann, K. Chan and B. M. Weckhuysen, *ChemSusChem*, 2019, **12**, 3491–3500.
32 J. Y. Zhang, Y. Yan, B. B. Mei, R. J. Qi, T. He, Z. T. Wang, W. S. Fang, S. Zaman, Y. Q. Su, S. J. Ding and B. Y. Xia, *Energy Environ. Sci.*, 2021, **14**, 365–373.
33 C. Liu, W. Zhou, J. F. Zhang, Z. L. Chen, S. L. Liu, Y. Zhang, J. X. Yang, L. Y. Xu, W. B. Hu, Y. N. Chen and Y. D. Deng, *Adv. Energy Mater.*, 2020, **10**, 2001397.
34 J. Ma, M. Wang, G. Lei, G. Zhang, F. Zhang, W. Peng, X. Fan and Y. Li, *Small*, 2018, **14**, 1702895.
35 S.-H. Li, M.-Y. Qi, Y.-Y. Fan, Y. Yang, M. Anpo, Y. M. A. Yamada, Z.-R. Tang and Y.-J. Xu, *Appl. Catal., B*, 2021, **292**, 120157.
36 L. Yu, Q. Zhu, S. Song, B. McElhenny, D. Wang, C. Wu, Z. Qin, J. Bao, Y. Yu, S. Chen and Z. Ren, *Nat. Commun.*, 2019, **10**, 5106.
37 J. H. Kim, S.-K. Park, Y. J. Oh and Y. C. Kang, *Chem. Eng. J.*, 2018, **334**, 2500–2510.
38 Q. Quan, S. Xie, B. Weng, Y. Wang and Y.-J. Xu, *Small*, 2018, **14**, 1704531.
39 X. Ma, B. Wei, M. Yuan, J. Li, S. Liang, Y. Wu, D. Dai and L. Xu, *J. Mater. Sci.*, 2020, **55**, 6502–6512.
40 Y. Zhang, C. Liu, X. Gao, Z. Luo, J. Hu, G. Zou, H. Hou, Z. Xu and X. Ji, *Nano Energy*, 2020, **68**, 104333.
41 Z. Li, Y. Fu, J. Bao, M. Jiang, T. Hu, T. Liu and Y.-n. Xie, *Appl. Catal., A*, 2001, **220**, 21–30.
42 C. C. Williams, J. G. Ekerdt, J. M. Jehng, F. D. Hardcastle, A. M. Turek and I. E. Wachs, *J. Phys. Chem.*, 1991, **95**, 8781–8791.
43 Y. Li, W. Qiu, F. Qin, H. Fang, V. G. Hadjiev, D. Litvinov and J. Bao, *J. Phys. Chem. C*, 2016, **120**, 4511–4516.
44 C. Hess, *Chem. Soc. Rev.*, 2021, **50**, 3519–3564.
45 Y. Jiang, P. Sun, L. Sharma, B. Mao, R. Kakkar, T. Meng, L. Zheng and M. Cao, *Nano Energy*, 2021, **81**, 105645.

46 D. Zhao, K. Sun, W. C. Cheong, L. Zheng, C. Zhang, S. Liu, X. Cao, K. Wu, Y. Pan, Z. Zhuang, B. Hu, D. Wang, Q. Peng, C. Chen and Y. Li, *Angew. Chem., Int. Ed.*, 2020, **59**, 8982–8990.
47 Y. Jiang, X. Wu, Y. Yan, S. Luo, X. Li, J. Huang, H. Zhang and D. Yang, *Small*, 2019, **15**, e1805474.
48 C. Li, J.-W. Zhao, L.-J. Xie, Y. Wang, H. Tang, L. Zheng and G.-R. Li, *J. Mater. Chem. A*, 2021, **9**, 12659–12669.
49 H. Jin, X. Wang, C. Tang, A. Vasileff, L. Li, A. Slattery and S.-Z. Qiao, *Adv. Mater.*, 2021, **33**, 2007508.
50 L. Zhu, L. Sun, H. Zhang, H. Aslan, Y. Sun, Y.-D. Huang, F. Rosei and M. Yu, *Energy Environ. Sci.*, 2021, **14**, 2451–2459.
51 S. Dresp, F. Dionigi, M. Klingenhof and P. Strasser, *ACS Energy Lett.*, 2019, **4**, 933–942.

Published on 15 December 2021. Downloaded on 3/7/2022 5:58:32 AM.

This journal is © The Royal Society of Chemistry 2022